Introduction of a New Technique to Measure the Coefficient of Restitution for Nanoparticles

Christian Schöner[1],*, Stephan Rennecke[2], Alfred P. Weber[2], and Thorsten Pöschel[1]

A modified single-stage low pressure impactor is described to measure the coefficient of normal restitution e_n for nanoparticles. The device is analysed numerically using CFD, and the gas flow inside the structured impaction plate is studied. A formula for the calculation of e_n is derived and first measurements of e_n for spherical silver particles are presented together with numerical data obtained from force-based molecular dynamics simulations. Furthermore, the simulation data for e_n and the sticking probability are investigated in detail for the elastic, and partly for the plastic impaction regime.

1 Introduction

Interactions of particles, with a size below $1\,\mu m$, with surfaces are important for understanding a variety of processes of technical or natural origin. In such processes, the collection of particles is often desired for filtration or coating applications. However, nanoparticles are also employed in surface modifications, e.g., the polishing of semiconductor surfaces, where a detachment of the particles is favorable. Particle collisions are of great importance for the modeling of fundamental processes in a wide range of interests, from agglomeration up to the understanding of the formation of planets and planetary rings [1]. Particle surface interactions are commonly described by the coefficient of normal restitution e_n, which is the ratio of the normal component of the particle's relative velocity after and prior to the collision. When colliding at low impact velocity, nanoparticles stick to adhesive surfaces upon contact, due to the prevalence of the freed adhesion energy compared to the kinetic energy of the center of mass. Consequently, $e_n = 0$ for such impacts up to a critical impact velocity v_{cr} sufficient to overcome adhesion and allow post-collisional detachment from the surface [2–4]. Experimental values of v_{cr} for sodium chloride and silver nanoparticles were recently published by [5]. It was found that in vacuum, the onset of particle rebound occurred at moderate impact velocities of several meters per second. At atmospheric conditions bigger impact velocities are necessary as the drag force reduces the particle stopping distance

after rebound to the length scale of van der Waals interactions [6]. This leads to a bigger apparent adhesion force and increased v_{cr}. For big impact velocities ($v_i > 20\,\mathrm{m\,s^{-1}}$), adhesion becomes negligible, and e_n is determined by the energy loss of the particle during contact. Kinetic energy can be dissipated in different forms, such as plastic deformation, temperature increase or restructuring mechanisms.

The rebound behavior of particles was object of extensive research and a variety of impact models were developed. In [2], the authors proposed a purely elastic model for the calculation of e_n that was later validated for polystyrene spheres colliding with a quartz substrate [7]. Plastic deformation was considered by [8]. The role of adhesion on particle rebound was investigated by [9] through the inclusion of the JKR theory into their model [10]. Other mentionable models include the role of surface roughness, dynamic yield stress or oblique impact [11–17]. In the last decade, the analysis of particle/wall interactions was complemented with the results of MD simulations [18–26]. These simulations allow an insight into aspects that are not covered by continuum mechanical models, such as the role of dislocations, elasto-plastic deformation, temperature increase or phase transition plasticity. For the measurement of the particle velocities of particles in the micrometer size range, established measurement techniques such as laser Doppler anemometry (LDA) are available. In contrast, for nano-sized particles, so far nearly no experimental data has been published for the coefficient of restitution. The only collection of experimental data for e_n was published by [27], who employed an indirect approach to determine e_n for 20 nm bismuth particles. A beam of the particles was impacted with a given velocity into a V-shaped template etched into a silicon wafer. The particles were reflected at one side of the V-shape before sticking to the other side. The height of the resulting characteristic distribution of the particles within the shape could then be measured to calculate e_n. It shows that information about

[1]Christian Schöner (christian.schoener@cbi.uni-erlangen.de), Prof. Thorsten Pöschel, Institut für Multiscale Simulation, Friedrich-Alexander University of Erlangen-Nürnberg, Nägelsbachstraße 49b, 91052 Erlangen, Germany; [2]Stephan Rennecke, Prof. Alfred P. Weber, Institute of Particle Technology, Technical University Clausthal, Leibnizstraße 19, 38678 Clausthal-Zellerfeld, Germany.

the rebound behaviour can be gained without direct measurements of the particle velocity.

In the first part of this paper, an approach for the measurement of e_n is presented, based on the impaction of size selected nanoparticles in a modified single-stage low pressure impactor (SS-LPI). LPIs were already successfully employed to investigate the breakup of nanoparticle agglomerates upon impact loading [28, 29], the phase state of atmospheric aerosol particles [30–32], as well as the rebound and charging behavior of single particles [5, 33] and agglomerates [34]. The feasibility of impact experiments with controlled impact velocity was recently shown by [35]. This method is extended to the direct determination of e_n by the introduction of an impaction void that determines the particle impulse necessary to leave the SS-LPI. Based on CFD analysis, a mathematical model for the direct calculation of e_n is proposed.

In the second part of this paper, measurements of the coefficient of restitution for dense spherical silver particles are presented together with data obtained by a numerical study based on force-based molecular dynamics (MD). Using the EAM (*embedded atom method*) potential to describe the interactions between the atoms of the particle, it is possible to reproduce the experimentally measured values for e_n. A detailed analysis of the impact velocity and particle size dependency of e_n and the sticking probability was then performed based on the simulation data.

2 Setup of the Experiments and Simulations

2.1 Experimental Prerequisites – Low Pressure Impaction and the Impaction Void

Determining the coefficient of restitution requires knowledge of the incident and rebound velocity, v_i and v_r, respectively. A direct measurement of the velocity of small particles below 100 nm in diameter is not possible yet at the required length scales. Therefore, indirect methods to determine the particle velocity have to be used. For collision experiments in a SS-LPI the incident velocity of a rebounding particle can be calculated from the process parameters and the particle properties using the following three parameter model:

$$U_{imp} = U_{max}(p)\,\bar{U}_{imp}\left(Stk^*,\frac{L}{D}\right)\chi_{lag}$$
$$\left(Stk^*,\frac{L}{D},\frac{H}{D}\right) \tag{1}$$

where U_{max} is the maximum gas velocity at the accelerating nozzle

outlet, $\bar{U}_{imp}$ the non dimensional impact velocity at a given Stokes number Stk* and the correction function χ_{lag} accounting for the lag of particles. L, H and D denote geometrical dimensions of the LPI as indicated in Fig. 1. Note that Stk* is modified compared to the classical definition and given by:

$$Stk^* = \frac{2\rho_p d_p^2 C_C U_{max}}{9\mu D} \tag{2}$$

where ρ_p is the particle density, d_p its diameter, C_c denotes the slip correction factor and μ is the viscosity of the surrounding gas. U_{max} is calculated assuming an ideal and incompressible gas, as well as a parabolic velocity profile at the nozzle outlet. In order to correct U_{max} for dynamic pressure losses in the near compressible regime, it was calculated at stagnation conditions following the Bernoulli equation. The non-dimensional impact velocity $\bar{U}_{imp}$ can be written as follows:

$$\bar{U}_{imp} = \frac{-B}{Stk^* + A} + 1 \tag{3}$$

where the empirical constants A and B depend on the L/D ratio and are 0.328 and 0.692, respectively. The factor χ accounts for insufficient acceleration of the particles and is given by:

$$\chi = 1 - 0.58\exp\left(-\frac{\bar{S}/\bar{S}_{99}}{0.19}\right) - 0.32\exp\left(-\frac{\bar{S}/\bar{S}_{99}}{0.022}\right) \tag{4}$$

with the non-dimensional stopping distance:

$$\bar{S}_{99} = \frac{4\tau U_{max}}{D} = 2Stk^* \tag{5}$$
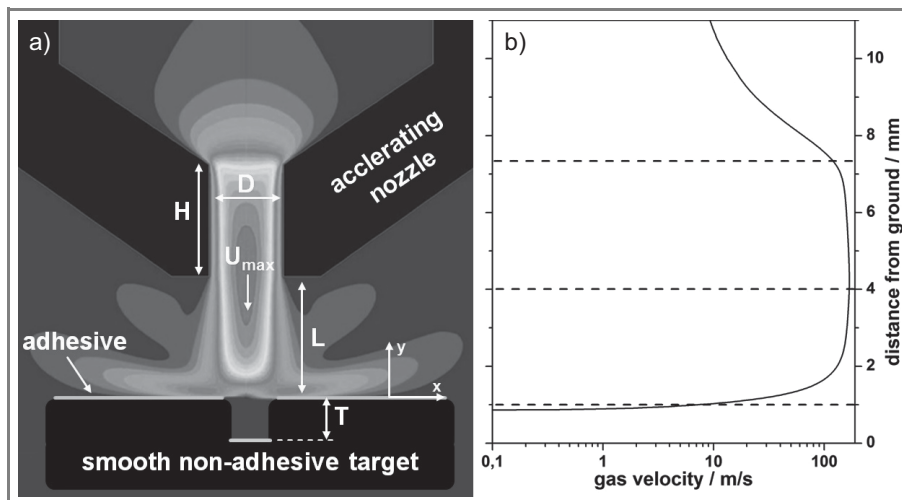
Figure 1. Schematic representation of the modified SS-LPI with impaction void (a) and gas velocity profile at the axis of symmetry (b).

and the necessary acceleration length:

$$\bar{S} = \frac{H+L}{D} - 0.5 \tag{6}$$

The result of this model is the particle impact velocity for a planar target. However, the rebound velocity cannot be determined following these methods. The approach presented in this work was to determine the rebound velocity of a particle through the introduction of a stagnation domain to the impaction target. (Fig. 1a). The particle will be accelerated analogous to standard right angle impaction in the gas jet, but instead of hitting the plate, it will enter the void filled with stagnant gas. Due to particle drag, the gas leads to a further deceleration of the particle before it hits the ground, where it possibly rebounds. After rebound the particle has to acquire enough momentum to cross the void once more. In this case, the particle will be re-suspended in the main stream of the impactor stage and can be detected at the outlet. Otherwise the particle will be captured in the void where diffusion will transport it quickly to the wall. In such a system the necessary momentum to leave the void can be easily defined by adjustment of its depth T.

A key condition for this method is a stagnant gas in the void. In order to prove that the gas motion inside the void is negligible, a CFD analysis was performed. The details of the numerical simulation were recently described elsewhere [35] and are standard knowledge of aerosol technology. As a result, it was found that the assumption of stagnant gas is fulfilled when the diameter of the void is significantly smaller than the accelerating nozzle, e.g., $0.5D$. An example of a gas velocity profile on the axis of symmetry of a SS-LPI ($D = 2\,\text{mm}$, $T = 1\,\text{mm}$ and diameter of the void $0.5D$) is shown in Fig. 1b. After the gas in the nozzle is accelerated to U_{max}, it is sharply redirected at the impaction target. Consequently, the gas velocity drops to zero directly at the inlet of the void. Further analysis reveals that a laminar vortex of negligible velocity is formed inside the void, which is separated from the main gas flow.

Assuming a perfectly stagnant gas in the void, and no effect of the void on the main flow, the particle velocity at the inlet of the void $v_i(0)$ can be calculated according to the model developed for conventional right angle impaction. Nanoparticles moving in a low pressure environment usually exhibit a low particle Reynolds number, and thus, are moving in the Stokes regime. As there is a linear relationship between particle velocity and travelled distance, this allows a simple extrapolation of the particle velocity into the void. Consequently, the impact velocity at the ground of the void can be written as:

$$v_i(-T) = v_i(0) - \frac{T}{\tau(p)} \tag{7}$$

If $v_i(-T)$ exceeds v_{cr} the particle will rebound with a certain velocity v_{cr}. The rebounding particle will be able to leave the void if its stopping distance S is larger than T:

$$S = \tau v_r \geq T \tag{8}$$

The rebound velocity can be expressed by the coefficient of normal restitution:

$$\tau v_i(-T) e_n \geq T \tag{9}$$

Finally, by substituting Eq. (7) into Eq. (9) and upon rearrangement the following is obtained:

$$e_n = \frac{T}{\tau(p) v_i(0) - T} \tag{10}$$

Thus, the coefficient of normal restitution can be determined by measuring the impaction pressure when particles first leave the void. The evaluation procedure will be presented in more detail in the results section.

2.2 Experimental Setup

The characteristics of the modified SS-LPI were investigated through the impaction of size-selected, spherical silver particles. The employed setup is schematically shown in Fig. 2. Silver nanoparticles were continuously produced by evaporation of silver electrodes in a spark discharge generator. The formed fractal agglomerates were transported through a tube furnace, heated to $550\,°\text{C}$, where they sintered to dense spheres. After passing a radioactive Kr^{85} neutraliser the particles were size selected according to their mobility in a radial differential mobility analyser (R-DMA). The singly charged, size selected particles subsequently entered the SS-LPI. Inlet and outlet concentration of the particles were monitored with Faraday cup electrometers (FCE). The impaction pressure, determining the gas velocity U_{max} in Eq. (1), was varied continuously from small to large pressures at a constant rate.

For this purpose a 100-L pressure reservoir was attached to the outlet of the SS-LPI. The impaction pressure was initially decreased to around $8\,\text{mbar}$ with a vacuum pump before the pump was disconnected with a valve. Subsequently, the pressure increased due to the constant aerosol mass flow into the SS-LPI, determined by the critical orifice at the inlet ($200\,\mu\text{m}$). This setup allows a quasi-steady recording of the particle penetration through the device at high resolution. The high resolution is crucial for the determination of e_n as Eq. (10) is very sensitive to the pressure. The penetration efficiency ε through the device was calculated from the FCE-signals as follows:

$$\varepsilon(p) = \frac{c_{\text{inlet}}/c_{\text{outlet}}}{c_{\text{inlet},0}/c_{\text{outlet},0}} \tag{11}$$

The measurement was stopped when the impaction pressure was too high for particle deposition to occur and the resulting ratio of inlet and outlet signal $c_{\text{inlet},0}/c_{\text{outlet},0}$ was used for normalization in order to account for diffusion losses as stated in Eq. (11). The impaction void was realized with an aluminium piston attached to a micrometer screw that was movable in the impaction target (Fig. 3). The im-
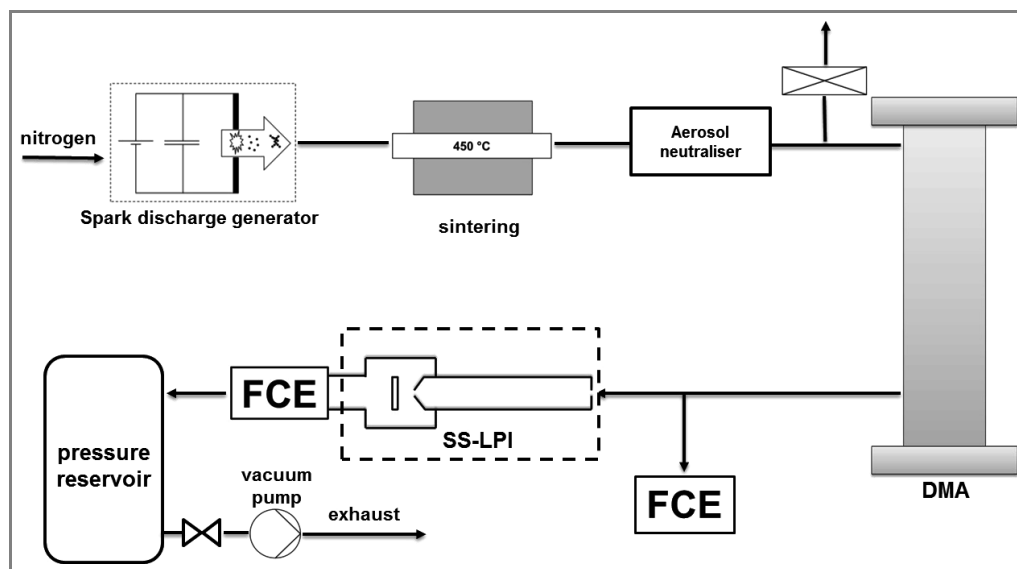
Figure 2. Schematic representation of the experimental setup.
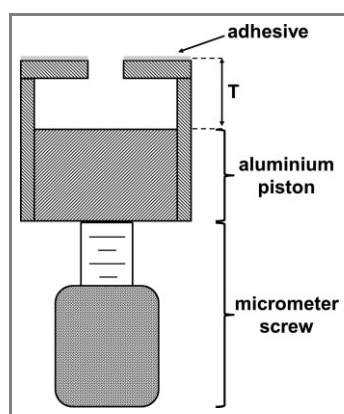
Figure 3. The practical implementation of the impaction void with adjustable depth.

paction target itself was covered with vacuum grease to avoid any particle rebound outside void. The diameter of the void was half of the nozzle diameter, e.g., 1 mm for the 2 mm accelerating nozzle.

The thickness of the upper shell was 350 µm, determining the minimum value of T. Note that 0.1 mm were added to the value of T in the calculation of e_n in order to account for the thickness of the grease film. The attached micrometer screw allowed the continuous variation of T with an uncertainty of 10 µm. The void forming beneath the upper shell has a bigger diameter than the opening, for two reasons: Particles rebounding from surface irregularities with a strongly changed angle cannot jump out of the void. This assures that the measured value of e_n corresponds to the normal case. Secondly, the bigger volume makes it more likely that particles not impacting on the ground of the void are caught, and do not contribute to the noise of the measurement arising from back diffusion. This is discussed later on.

2.3 Experimental Deposition Characteristics

In order to investigate the influence of the impaction void on the deposition characteristics of silver particles, the penetration was measured and compared to the deposition on a conventional plane impaction target. For this experiment the ground of the void was also covered with vacuum grease. The results for 600 nm particles are shown in Fig. 4.

At high impaction pressures above 70 mbar the signal is the same for both curves, since all particles pass through the SS-LPI without impaction. In case of a planar impaction target (solid line), the signal decreases with decreasing impaction pressure as the particles exhibit sufficient inertia to be captured by the grease film, and finally drops to zero.
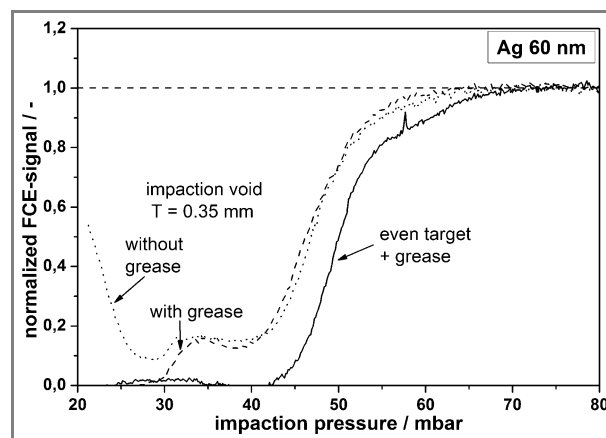
Figure 4. Penetration of silver particles through the SS-LPI with planar (solid line) and structured (dashed line) impaction target, both covered with vacuum grease. Additionally, the penetration for allowed particle rebound at the ground of the void is included.

www.cit-journal.com

© 2014 WILEY-VCH Verlag GmbH & Co. KGaA, Weinheim

Chem. Ing. Tech. 2014, 86, No. 3, 1–11

The curve exhibits the typical sigmoidal shape. In case of impaction target with impaction void, the signal exhibits the same shape but with a shift to lower impaction pressures. Instead of dropping to zero, the signal exhibits a plateau between 30 and 40 mbar before dropping to zero at lower pressures. Particle deposition occurs first for particles moving in the middle of the gas jet because these particles exhibit the highest gas velocity. Consequently, particles that are accelerated with a higher radial position in the gas jet are deposited last. When the impaction void is present in the core of the gas jet, there is no surface for particle capture available. At high pressure, when deposition just occurs, the relative displacement of the particles to their streamline is not sufficient to move the particles into the void. Thus, no particle capture occurs and the deposition curve is shifted to smaller pressures where the impaction pressure is sufficient to deposit particles with higher radial position. At pressures below 40 mbar, when all particles are deposited in the planar case, a plateau is forming. This noise with a magnitude around 0.17 is observed in every measurement and is a consequence of back diffusion of the particles from the void to the main flow. At even lower impaction pressures, when the particles reach the ground of the void and are captured by the grease film, the signal finally drops to zero. These cases are also schematically shown in Fig. 5a and 5b.
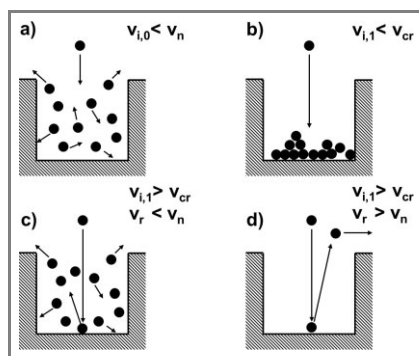
Figure 5. Schematic representation of the different stages of particle deposition in the impaction void. a) Particles do not reach the ground; b) particles reach the ground, but are captured; c) particles rebound from the ground, but don't leave the void; d) particle rebound and re-suspension in the main flow.

In Fig. 4 the case of allowed particle rebound in the void (dotted line, no grease in the void) is also included for comparison. The signal follows the case of deposition perfectly above 30 mbar. For smaller impaction pressure the signal does not drop to zero as particle rebound occurs. In direct measurements for silver particles, v_{cr} was found to be smaller than $0.5 \, \text{m s}^{-1}$ for 60 nm particles. This value is exceeded quasi instantaneously after the onset of deposition at the ground of the void. However, at pressures near 30 mbar the rebound velocity of the particles is insufficient to leave the void (Fig. 5c). Consequently, the particles accumulate and back diffusion occurs to a lesser extend than in case b), since both case b) and c) take place simultaneously. At im-

paction pressures smaller than 26 mbar the rebound velocity is sufficient to jump out of the void (Fig. 5d), allowing the calculation of e_n according to Eq. (10). However, the actual values of e_n will be discussed in Sect. 3.2.

The signals for 60 nm silver particles impacting into a void of variable depth are plotted in Fig. 6. T was varied between 3.35 and 0.95 mm. For impaction pressures above 30 mbar, where the depth of the void has no influence on the deposition behaviour, the different signals are congruent. With increasing depth T of the void the pressure necessary for particle release after bounce decreases.
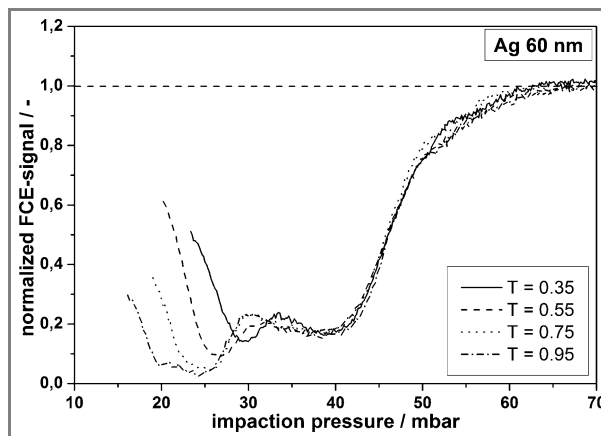
Figure 6. Penetration of 60-nm silver particles through the SS-LPI equipped with an impaction void of variable depth T.

While rebound from the void is visible at 30 mbar at a depth of 0.35 mm, the pressure has to be decreased by 10 mbar to observe rebound at $T = 0.95$ mm. It is also obvious that the plateau value close to the onset of the bounce decreases. This is due to the larger volume of the void, making back-diffusion to the main gas flow less likely. However, the signal magnitude from the rebounding particles is also reduced with increasing T. From the measurements performed so far it was found that particle rebound is detectable for values of T up to 1.1 mm. Changes of T as small as 50 μm are reliably detectable.

2.4 Simulation Setup

For the impact simulations, which were carried out as force-based MD calculations, two different models were used to describe the interaction. Between the atoms of the particle the EAM-model was used, for which the energy of a given atom reads

$$E_{i,\text{EAM}} = F\left(\sum_{j \neq i} \rho(r_{ij})\right) + \frac{1}{2} \sum_{j \neq i} \phi(r_{ij}) \qquad (12)$$

F is the embedding energy functional, ρ the atomic electron density function and ϕ a pair potential interaction. This

model is reliable in reproducing the main properties of bulk crystals [36]. Tabulated values for silver were chosen to carry out the simulations. For the interaction between wall atoms and particle atoms a cut off and smoothed Lennard-Jones-Potential was applied:

$$E_{i,LJ} = 4\varepsilon \sum_{j \neq i} \left(\left(\frac{\sigma}{r_{ij}} \right)^{12} - C \left(\frac{\sigma}{r_{ij}} \right)^{6} \right) + C_1 r_{ij} + C_2 \qquad (13)$$

where ε is the depth of the energy well and σ the characteristic Lennard-Jones distance for which literature values for silver were chosen [37]. C is a constant to vary the strength of the attractive part of the energy. Here, 0.35 was used to simulate a weakly adhesive contact, taking into account the effect of a covering oxide layer onto the interaction strength. C_1, C_2 are constants to smooth out $E_{i,LJ}$ at the cutoff distance, for which $r_c = 2.5\sigma$ was chosen.

The wall is modelled ideally to be stiff, with no possibility for the atoms to move. Its structure is that of a cylindrical shaped fcc-grid, where the diameter and height of the cylinder are chosen in a way that boundary effects never occur during any of the simulations. For the distance between the atoms of the wall the zero force distance of the Lennard-Jones potential between the wall atoms and the particle atoms was selected.

The particle is initialized for the impacts by first cutting a ball out of a fcc-grid and then equilibrate it at 300 K using a Nosé-Hoover thermostat. A time step of $6 \cdot 10^{-16}$ s was used. Fig. 7 shows the initial positions of the impact system.
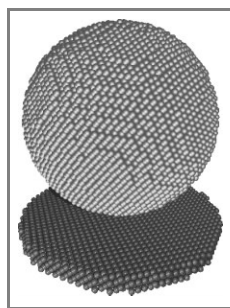
Figure 7. Initial state of the system just before the impact.

To start a simulation, the particle was placed just outside the Lennard-Jones interaction range, rotated and shifted randomly, and the desired impact velocity was added. The particle diameter was varied in the range of 2.5 – 15 nm and the impact velocity from 10 to 90 m s^{-1} in steps of 5 m s^{-1}. The simulations were carried out for 100 random rotations for each particle diameter and each impact velocity since the impacts are heavily dependent on the rotational state of the particle and its tangential position above the wall.

3 Results and Disussion

3.1 Phases of the Impact

A typical impact with rebound occurs in 4 phases as shown in Fig. 8. The data is taken from a simulation of a 5 nm particle.
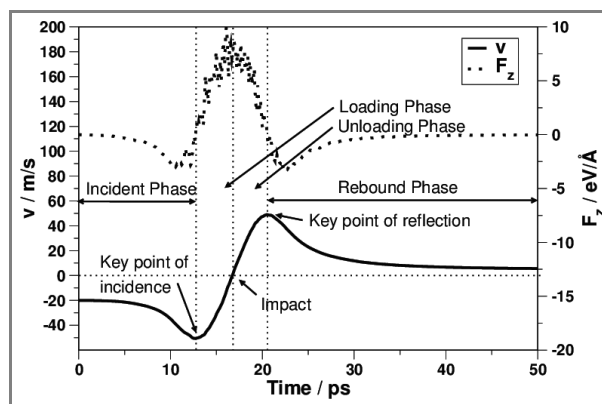
Figure 8. Phases of the impact.

In the beginning, during the incident phase, there are only attractive forces acting between wall and particle, therefore, the particle is accelerated towards the wall. When the distance becomes smaller, the atoms closest to the wall are subject to repulsive forces and the center of mass becomes decelerated as soon as the overall force becomes repulsive, marking the key point of incidence. From here on, the kinetic (center of mass) energy of the particle is completely converted into potential energy, charaterizing the loading phase. The center of mass velocity then passes 0, the actual impact event, since in this moment the particle stands still over the wall. Afterwards, the repulsive forces lead to an acceleration of the particle away from the wall, redistributing the potential energy from the loading phase into the available degrees of freedom in the unloading phase. At some distance, the attractive contribution to the force between wall and particle is again larger than its repulsive counterpart. Therefore, the particle is decelerated starting from this key point of reflection in the rebound phase. Finally, after escaping the range of interaction, the trajectory of the particle is not affected by the wall anymore. In the following, if speaking of taking only the loading/unloading phases into account, the collision parameters at the key point of incidence and the key point of reflection are looked at. On the other hand, if speaking of the full adhesive contact, the collision parameters at the beginning of the incidence phase and the end of the rebound phase are considered.

3.2 The Coefficient of Normal Restitution for Silver Nanoparticles

The coefficient of normal restitution e_n for Ag-particles in the $18-66$ nm size range was calculated from experimental data using Eq. (10). The pressure at which particles first rebound out of the void was determined by fitting a straight line to the linear part and calculating the intersection with the respective plateau. The geometric depth of the void was varied between 0.35 and 1.05 nm in steps of 100 μm. For a given particle size, the complex interplay between pressure, impact velocity and stopping distance allowed only a limited impact velocity range to be correct. Therefore, in order to explore a larger velocity range, particles of different sizes were investigated. A variation of T in the stated impact velocity range results in impact velocities between 30 and 90 m s^{-1}. Each void depth results in the measurement of one individual value of e_n where the impact velocity cannot be predicted. An increase in T at a given impaction pressure results in a decrease of impact velocity and an increase in the necessary rebound velocity. The results of these measurements are plotted together with the numerical results for 15 nm particles in Fig. 9.

The experimentally measured coefficient of normal restitution exhibits values around 0.9 for v_i at 30 m s^{-1} and decays to nearly 0.5 at 90 m s^{-1} with increasing v_i. Although the diameter of the Ag-particles is varied by a factor of more than 3, the measured coefient of normal restitution agrees within experimental uncertainties. Therefore, e_n can, at least as a first approximation, be considered as independent of particle size.

The numerical results for 15 nm coincide well with the measured values, impliying comparability of experimental and numercial results for the case of strong reflection of the normal part of the kinetic energy, i.e., for weakly adhesive

contacts of silver nanoparticles in the mostly elastic part of the plastic regime.

However, for particle sizes below 15 nm, it was observed in the simulation that e_n is strongly dependent on particle size (Fig. 9). With increasing size, surface effects get less dominant compared to volume effects, thus, the graph for the full adhesive contact and the graph taking only the loading/unloading phase into account approach each other. A maximum for the coefficient of restitution can be found for every tested particle diameter and impact velocity range. This can be explained by the following rationale: For low impact velocities, the (tangential) acceleration of the particle due to attractive forces plays a major role. On the one hand, an increase in impact velocity makes this effect less important, therefore resulting in an increase of e_n. On the other hand, an increase of the impact velocity also leads to a stronger deformation, which is accompanied by dissipation, thereby redirecting kinetic energy in normal direction into inner degrees of freedom (temperature and potential energy). Furthermore, stronger deformation leads to higher adhesion energy, and as a result e_n decreases. It is oberved that these processes balance each other at about $55-60$ m s^{-1}, where the maximum of e_n is situated. Since adhesive acceleration effects play a less important role for increasing mass, the role of the e_n-increasing effect (on the left of the maximum) becomes more important for increasing particle size, leading to a steeper slope when comparing the curves for the different, tested particle diameter. The amount of energy to plastically deform the particle locally depends on local grid structure, which is independent of the mass of the particle. Thus, for increasing particle size the same amount of kinetic energy acting on the main impact area of the particle is reached for smaller values of v. Therefore, for increasing particle diameter the maximum of e_n is shifted towards lower values of impact velocity.
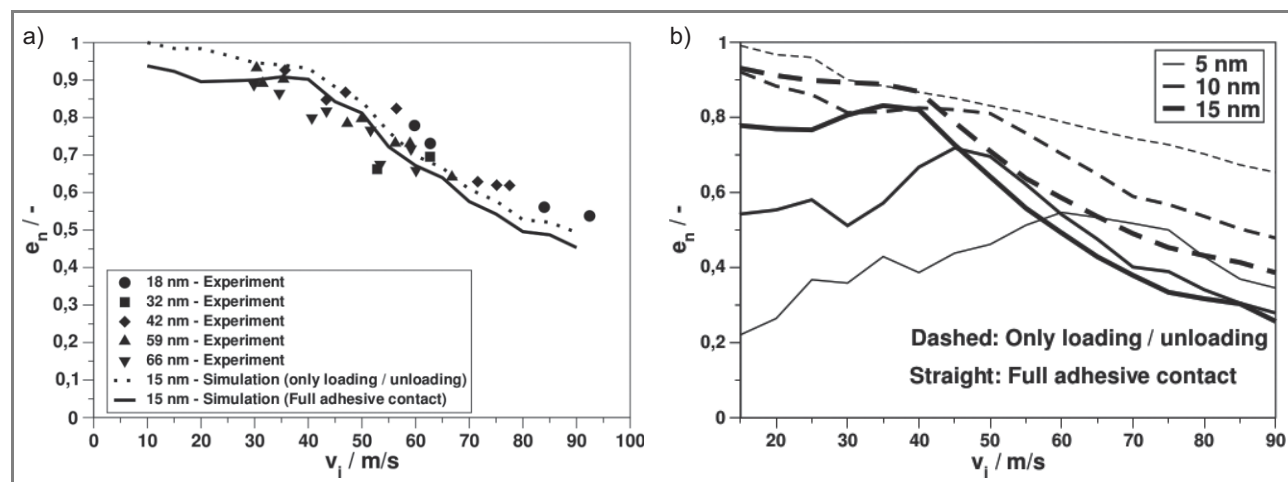
Figure 9. a) Measured and numerically calculated 95-percentiles for various particle sizes; b) coefficient of normal restitution obtained from simulation.

3.3 The Sticking Probability

The measured sticking probability (Fig. 10) is in agreement with the works of other authors working on this field [18, 19, 23]. First the graph for 5 nm will be discussed. At the lowest impact velocity of $10\,\mathrm{m\,s^{-1}}$, a sticking probability of 100 % was observed. This behaviour can be explained by the fact that for low impact velocities, the kinetic energy of the particle in normal direction at the key point of reflection is lower than the corresponding adhesion energy. So except for rare cases of thermal rebounds, where additional amounts of thermal and potential energy are utilized during the escape trial process (which will be excluded for the rest of this investigation), the particle sticks for all possible rotations and shifts of the center of mass tangential to the wall prior to the collision. With increasing impact velocity, the kinetic energy increases quadratically, but the forementioned adhesion energy stays more or less constant (Fig. 10). At some point, the reflected kinetic energy exceeds the adhesion energy, which gives the possibility of rebounce. Here, this is already the case for velocities lower than $10\,\mathrm{m\,s^{-1}}$. Since the adhesion energy at the key point of reflection is nearly independent of the impact velocity up to $60\,\mathrm{m\,s^{-1}}$, it is concluded that in this velocity range the impact takes place in a mostly elastic fashion.

The efficiency of the reflection of the normal part of the kinetic energy and thereby the sticking probability can be understood by the coefficient of normal restitution e_n together with the Weber number at the key point of reflection

$$\mathrm{We_{r*}} \equiv \frac{E_\mathrm{Kin,z,r*}}{E_\mathrm{Adh,r*}} \tag{14}$$

where the index $r*$ means absolute value of the energy at the key point of reflection. $\mathrm{We_{r*}}$ describes the ratio of available kinetic energy in normal direction and adhesion energy that needs to be invested to escape the orbit of the wall. At least a value of 1 is required to escape. Since the deformation process is not yet completed at the key point of reflecti-

on, it must be kept in mind that a part of this kinetic energy in normal direction is also redirected into the particle's potential energy, and that this redirection process is accompanied by dissipation.

The critical velocity v_cr is the lowest velocity for which a rebound of the particle from the wall may be observed. Thus, it can be characterized by $\mathrm{We_{r*}} = 1$. From the Fig. 10b it can be seen that $v_\mathrm{cr}^{5\mathrm{nm}} \le 10\,\mathrm{m\,s^{-1}}$, while the sticking probability alone would suggest a value bigger than $10\,\mathrm{m\,s^{-1}}$.

The sticking probability is then decreasing up to about $55-60\,\mathrm{m\,s^{-1}}$. This can be reasoned by the collision being mostly elastic: The loading/unloading process is linearly depending on impact velocity, whereas the kinetic energy scales quadratically and the tangential acceleration plays a less important role for increasing impact velocity. The adhesion energy at the key point of reflection stays more or less constant. Therefore, in this moment the shape of the particle is statistically the same in the velocity range up to $60\,\mathrm{m\,s^{-1}}$, resulting in more kinetic energy being available for the escape trial.

In analogy to the influence of plastic deformation on e_n, it results in an increase in sticking probability, too. Consequences are conversion of kinetic energy in normal direction into potential energy and dissipation of energy while doing so. Also, the amount of adhesion starts to increase as the impacted particle's shape becomes more pancake-like. The dissipation of energy due to the loading/unloading process starts to become more prominent (Fig. 9). The impact of plastic deformation thus leads to an increase of sticking probability, marking a change in regimes at $55-60\,\mathrm{m\,s^{-1}}$ impact velocity, from where on it increases.

By increasing the particle size, on the one hand, the adhesion energy scales with the square of the particle diameter, whereas its mass, and therefore its kinetic energy, scales with the third power. Thus, the excess of kinetic energy at the key point of reflection, compared to the corresponding adhesion energy, is increasing with particle size. Tangential acceleration and the redirection of kinetic energy from nor-
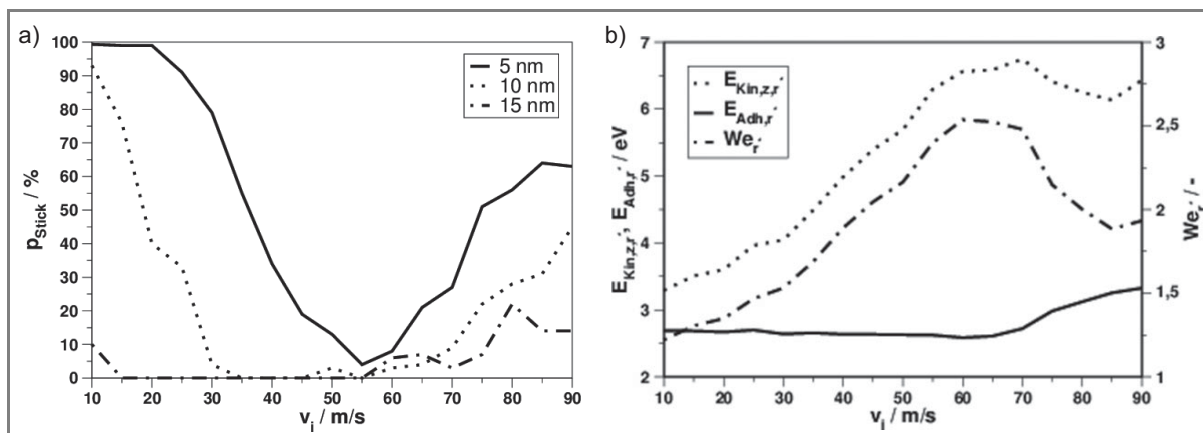
Figure 10. a) Sticking probability for various particle sizes; b) kinetic energy in normal direction and absolute value of adhesion energy at the key point of reflection for the impact of a 5 nm particle.

mal direction into tangential direction becomes less important and overall the slope of the sticking probability becomes steeper with increasing particle diameter (Fig. 9). As a result v_{cr} is decreasing with increasing particle diameter. On the other hand, in the regime dominated by plastic deformation, its increase does not scale with the third power of the particle diameter, since adhesion is a surface effect, and thus the slope gets less steep for bigger particles. From this follows that the sticking probability decreases at a given impact velocity with particle size, as is expected.

4 Conclusions

A method to measure the coefficient of normal restitution e_n was elaborated and the measured values for silver nanoparticles of sizes $18-60$ nm were reproduced numerically by force-based MD simulations. In case of silver, the experimental method is capable of measuring the coefficient of normal restitution for impact velocities down to $20\,\mathrm{m\,s^{-1}}$ and particle sizes down to approximately 20 nm. For lower velocities or smaller particles the method is limited since they have to exhibit a minimum impulse after rebound, which is mainly determined by the geometry of the void. Future work will concentrate on the extension of low pressure impaction-based determination of e_n for bouncing particles with lower impulse and particles undergoing oblique impacts. First measurements of e_n for silver particles are in reasonable agreement with numerical simulations. This shows for the first time that numerical impact simulations of nanoparticles can be viewed as a reliable tool in the prediction of properties of the impact events. In a first analysis the influence of adhesion on the coefficient of normal restitution and the sticking probability were investigated. The delivered results were satisfying and are well understood. For the future, it is planned to numerically investigate the influence of non-idealities of the particles and the wall on the contact as well as impacts with several particles involved, e.g., agglomerates.

Symbols used

C_c	[–]	slip correction factor
D	[m]	geometrical dimension of the LPI
d_p	[m]	particle diameter
$E_{kin,z}$	[J]	kinetic energy in z-direction
E_{adh}	[J]	adhesion energy
E_n	[–]	coefficient of normal restitution
L	[m]	geometrical dimension of the LPI

H	[m]	geometrical dimension of the LPI
p_{Stick}	[–]	sticking probability
Stk*	[–]	modified Stokes number
K	[m]	depth of the impaction void
U_{imp}	[m s^{-1}]	estimated particle velocity prior to the impact
$\overline{U}_{imp}$	[–]	dimensionless impact velocity
U_{max}	[m s^{-1}]	pressure dependent maximal gas velocity
v_{cr}	[m s^{-1}]	critical impact velocity for rebound
v_i	[m s^{-1}]	particle velocity prior to the impact
v_r	[m s^{-1}]	particle velocity after the impact
v_r^*	[m s^{-1}]	particle velocity at key point of reflection
We	[–]	Weber number

Greek symbols

ε	[–]	penetration efficiency
μ	[Pas]	dynamic viscosity of air
ρ_p	[kg m^{-3}]	particle density
τ	[m s^{-1}]	particle velocity before entering the void
χ_{lag}	[–]	lag factor

References

[1] H. Tanaka, K. Wada, T. Suyama, S. Okuzumi, *Prog. Theor. Phys. Suppl.* **2012**, *195*, 101–113.

[2] B. Dahneke, *J. Colloid Interface Sci.* **1971**, *37*, 342–353.

[3] S. Wall, W. John, H.-C. Wang, S. L. Goren, *Aerosol Sci. and Technol.* **1990**, *12*, 926–946.

[4] R. Brach, P. Dunn, X. Li, *J. Adhes.* **2000**, *74*, 227–282.

[5] S. Rennecke, A. P. Weber, *J. Aerosol Sci.* **2013**, *58*, 135–147.

[6] S. Rennecke, A. P. Weber, *J. Aerosol Sci.* **2013**, *58*, 129–134.

[7] B. Dahneke, *J. Colloid and Interface Sci.* **1973**, *45*, 584–590.

[8] L. Rogers, J. Reed, *J. Phys. D: Appl. Phys.* **1984**, *17*, 677–689.

[9] C.-J. Tsai, D. Y. H. Pui, B. Y. H. Liu, *Aerosol Sci. Technol.* **1990**, *12*, 497–507.

[10] K. L. Johnson, K. Kendall, A. D. Roberts, *Proc. R. Soc. London, Ser. A* **1971**, *324*, 301–313.

[11] S. Wall, W. John, *J. Aerosol Sci.* **1989**, *20*, 983–986.

[12] C. Thornton, K. Yin, *Powder Technol.* **1991**, *65*, 153–166.

[13] R. M. Brach, P. F. Dunn, *Aerosol Sci. Technol.* **1992**, *16*, 51–64.

[14] R. M. Brach, P. F. Dunn, *Aerosol Sci. Technol.* **1995**, *23*, 51–71.

[15] C. Thornton, Z. Ning, *Powder Technol.* **1998**, *99*, 154–162.

[16] W. Cheng, R. M. Brach, P. F. Dunn, *Aerosol Sci. Technol.* **2002**, *36*, 1045–1060.

[17] K. Johnson, H. Pollock, *J. Adhes. Sci. Technol.* **1994**, *8*, 1323–1332.

[18] A. Awasthi, S. C. Hendy, P. Zoontjens, S. A. Brown, *Phys. Rev. Lett.* **2006**, 97.

[19] A. Awasthi, S. C. Hendy, P. Zoontjens, S. A. Brown, F. Natali, *Phys. Rev. B.* **2007**, 76.

[20] A. Awasthi, S. Hendy, S. Brown, *Math. Mech. Solids.* **2010**, *15*, 771–781.

[21] L. Han, Q. An, S. Luo, W. I. Goddard, *Mater. Lett.* **2010**, *64*, 2230–2232.

[22] P. Valentini, T. Dumitrica, *Phys. Rev. B.* **2007**, *75*, 224106.

[23] S.-C. Jung, D. Suh, W.-S. Yoon, *J. Aerosol Sci.* **2010**, *41*, 745–759.

[24] A. Tomsic, N. Markovi, J. B. C. Pettersson, *J. Phys. Chem. B.* **2003**, *107*, 10576–10582.

[25] M. Suri, T. Dumitrica, *Phys. Rev. B.* **2008**, *78*.

[26] S. Sato, D.-R. Chen, D. Y. Pui, *Aerosol Air Qual. Res.* **2007**, *7*, 278–303.

[27] A. Ayesh, S. Brown, A. Awasthi, S. Hendy, P. Convers, K. Nichol, *Phys. Rev. B.* **2010**, *81*.

[28] M. Seipenbusch, S. Froeschke, A. Weber, G. Kasper, *J. Proc. Mech. Eng.* **2002**, *216*, 219225.

[29] S. Froeschke, S. Kohler, A. Weber, G. Kasper, *J. Aerosol Sci.* **2003**, *34*, 275–287.

[30] A. Virtanen, J. Joutsensaari, T. Koop, J. Kannosto, P. Yli-Pirilä, J. Leskinen, J. Mäkelä, J. Holopainen, U. Pöschl, M. Kulmala, D. Worsnop, A. Laaksonen, *Nature* **2010**, *467*, 824–827.

[31] A. Virtanen, J. Kannosto, H. Kuuluvainen, A. Arffman, J. Joutsensaari, E. Saukko, L. Hao, P. Yli-Pirilä, P. Tiitta, J. Holopainen, J. Keskinen, D. Worsnop, J. Smith, A. Laaksonen, *Atmos. Chem. Phys.* **2011**, *11*, 8759–8766.

[32] E. Saukko, H. Kuuluvainen, A. Virtanen, *Atmos. Meas. Tech.* **2012**, *5*, 259–265.

[33] H. Kuuluvainen, A. Arffman, E. Saukko, A. Virtanen, J. Keskinen, *J. Aerosol Sci.* **2013**, *55*, 104–115.

[34] M. Ihalainen, T. Lind, T. Torvela, K. E. J. Lehtinen, J. Jokiniemi, *Aerosol Sci. Tech.* **2012**, *46*, 990–1001.

[35] S. Rennecke, A. Weber, *J. Aerosol Sci.* **2013**, *55*, 89–103.

[36] M. S. Daw, M. I. Baskes, *Phys. Rev. B.* **1984**, 29.

[37] T. Halicioglu, G. M. Pound, *Phys. Status Solidi A* **1975**, *30*, 619–623.

Introduction of a New Technique to Measure the Coefficient of Restitution for Nanoparticles

C. Schöner*, S. Rennecke, A. P. Weber, T. Pöschel

Particle collisions are of great importance for the modeling of fundamental processes in a wide range of interests. So far it was not possible to determine the coefficient of restitution for nanoparticles experimentally. Here, a new measurement technique is described. The results are compared to and extended by a numerical study for detailed analysis. .... ■